International Journal of Solids and Structures 47 (2010) 1424–1434

Contents lists available at ScienceDirect

International Journal of Solids and Structures

journal homepage: www.elsevier.com/locate/ijsolstr

Cohesive modeling of crack nucleation under diffusion induced stresses in a thin strip: Implications on the critical size for flaw tolerant battery electrodes

Tanmay K. Bhandakkar, Huajian Gao *

Division of Engineering, Brown University, Providence, RI 02912, USA

ARTICLE INFO

Article history:
Received 2 December 2009
Available online 19 February 2010

Keywords:
Intercalation–deintercalation
Diffusion induced stress
Lithium electrodes
Fracture
Flaw tolerance
Cohesive zone

ABSTRACT

Recent advances in lithium-ion battery electrodes with huge volume changes during intercalation–deintercalation cycles are calling for studies on crack nucleation under diffusion induced stresses. Here we develop a cohesive model of crack nucleation in an initially crack-free strip electrode under galvanostatic intercalation and deintercalation processes. The analysis identifies a critical characteristic dimension below which crack nucleation becomes impossible. The critical size and other predictions of the model are compared to recent experiments on silicon nanowire electrodes. The results suggest nanostructured electrodes are highly promising for applications in high capacity batteries.

1. Introduction

It has been recognized that the development of damage tolerant battery electrodes for high capacity energy storage will be a critical step to meet the future energy needs of humanity. Lithium-ion (Li-ion) battery cells are now the most widely used secondary battery systems for portable electronic devices due to their high energy density, high operating voltages, low self-discharge, and low maintenance requirements compared to conventional aqueous rechargeable cells such as nickel–cadmium and nickel metal hydride (Tarascon and Armand, 2001). Li-ion batteries are based on the classical intercalation reaction during which lithium is inserted into or extracted from both cathode and anode. Significant research has been directed towards finding materials with ever greater capacity for accommodating Li atoms to increase battery efficiency (Thomas, 2003). Graphitized carbon, the most common anode for Li-ion batteries, exhibits relatively small volumetric change, stable working voltage and good cycle performance. However, the chemical compound LiC_6 limits the theoretical capacity of Li-C anodes to 372 mA h g^{-1} (Dahn et al., 1995), which is deemed insufficient for high power applications (Kim et al., 2006). Compared to the Li-C anodes, a variety of Li-alloy (Li_xM, M = Sn, Si, Ge, Al) anodes show substantially higher theoretical capacity, high Li packing density and safe thermodynamic potential (Kim et al., 2006). For example, as a potential candidate for anode in Li-ion batteries, silicon has a theoretical capacity of 4200 mA h g^{-1} with the formation of $Li_{4.4}Si$ alloy (Boukamp et al., 1981), which is substantially higher than that of carbon (Laforge et al., 2008). However, Si electrodes suffer from serious irreversible capacity and poor cyclability due to huge volume changes associated with the lithium ion insertion/extraction processes. This volume change compounded by high Li packing density often results in fast disintegration (cracking or 'crumbling') of the material (Yang et al., 1996; Winter et al., 1998; Bourderau et al., 1999). This phenomenon, commonly referred to as "decrepitation", has become a major obstacle for practical applications of Si and other high capacity materials in rechargeable Li-ion batteries. Existing strategies to prevent decrepitation of Si have mainly focused on using composite materials and reducing the alloy particle size. In the former approach, an electrochemically active phase is homogeneously dispersed within an electrochemically inactive matrix (Mao et al., 1999; Kim et al., 2000, 2006), with the inactive phase designed to accommodate the large strains generated by the active phase while maintaining the structural integrity of the composite electrode during the alloying/de-alloying processes. In the latter approach, the emphasis is on reducing the size and experimenting with the geometry of the electrode. It has been shown that cracking of Li_xSn can be avoided in multiphase anodes with small particle sizes (Besenhard et al., 1997). Nanostructured Si and Ge thin films exhibited superior performance during charge/discharge cycling compared to their bulk counterparts (Graetz et al., 2003, 2004). Anodes made of Cu nanorods plated with Fe_3O_4 showed an improvement by a factor of six in power density over planar electrodes while maintaining the same discharge time (Taberna et al., 2006). Recently, silicon nanowire electrodes of diameter less

* Corresponding author. Tel.: +1 401 8632626; fax: +1 401 8639025.
E-mail address: Huajian_Gao@Brown.edu (H. Gao).

0020-7683/$ - see front matter © 2010 Elsevier Ltd. All rights reserved.
doi:10.1016/j.ijsolstr.2010.02.001

than 100 nm have been found to accommodate volumetric strains as large as 400% without pulverization, while maintaining a discharge capacity close to 75% of its theoretical capacity with little fading during cycling (Chan et al., 2008). These experiments are strongly suggesting that size reduction is an effective strategy in creating fracture resistant, high capacity battery electrodes.

In the literature, the insertion/extraction of Li in an electrode has often been modeled as diffusion of interstitial atoms at the continuum level (García et al., 2005; Christensen and Newman, 2006a,b; Zhang et al., 2007; Cheng and Verbrugge, 2009). Most of the existing studies have focused on analysis of stresses induced by the diffusion of Li in a host particle, a subclass of problems more broadly referred to as the diffusion induced stresses (DIS) (Prussin, 1961; Li, 1978; Yang, 2005; Zhang et al., 2007; Cheng and Verbrugge, 2008, 2009). Christensen and Newman (2006a,b) studied stress generation in Li insertion into carbon anode and $LiMn_2O_4$ cathode particles. Zhang et al. (2007) performed detailed numerical studies of DIS in ellipsoidal $LiMn_2O_4$ particles under galvanostatic Li insertion and extraction, with results suggesting that particles with smaller sizes and larger aspect ratios lead to smaller intercalation-induced stresses. Cheng and Verbrugge (2009) have developed analytical expressions for the evolution of stress and strain energy within a spherical particle under both galvanostatic and potentiostatic conditions. It has also been shown that surface tension and surface modulus could significantly reduce DIS in nanosized particles (Cheng and Verbrugge, 2008).

In spite of the extensive studies of DIS in structures of various geometries, relatively few theoretical studies have explicitly considered the mechanisms of crack nucleation and propagation. Huggins and Nix (2000) considered a bilayer plate structure in which the top layer is subjected to a swelling transformation strain while the bottom layer contains a pre-existing crack. They showed that the swelling in the top layer causes a biaxial tensile stress in the bottom layer and used the Griffith criterion to predict a terminal thickness of the plate below which the pre-existing crack will not propagate.

Experiments have shown that crack nucleation usually occurs during the first intercalation–deintercalation cycle for the high capacity electrodes. However, the condition for crack nucleation under diffusion induced stresses in an initially crack-free electrode has not been addressed previously. Motivated by the increasing importance of this problem, here we develop a cohesive model of crack nucleation under diffusion induced stresses in a thin strip under galvanostatic charge and discharge. Compared to the Huggins–Nix model (Huggins and Nix, 2000), the electrode in our analysis is assumed to be initially crack-free, and the dynamic evolution of DIS and crack nucleation under galvanostatic (constant current) charging/discharging conditions will be explicitly modeled.

Cohesive models of fracture were originally developed to remove crack-tip stress singularity due to cohesive interactions (Barenblatt, 1959) or plastic deformation (Dugdale, 1960). This approach has also been extensively used to model crack nucleation in an initially crack-free material. For example, Needleman (1987) developed a cohesive model to describe void formation from initial particle debonding through complete separation to subsequent void growth. Camacho and Ortiz (1996) have applied cohesive models to describe dynamic fragmentation in an initially crack-free solid subject to impact. Mohammed and Liechti (2000) developed cohesive models of crack nucleation at bimaterial corners in aluminum-epoxy specimen under 4-point bending. In such models, a traction–separation law is assumed to act between separating surfaces and the criterion of crack nucleation is based on the maximum surface separation within the cohesive zone reaching a critical value. The most widely used traction–separation laws include rectangular (Dugdale, 1960), polynomial/exponential (Needleman, 1987), trilinear (Tvergaard and Hutchinson, 1992) and triangular (Camacho and Ortiz, 1996) law. Here we will adopt the triangular traction–separation law (Camacho and Ortiz, 1996) in modeling crack nucleation under DIS. In this model, if the maximum stress in the electrode is less than the cohesive strength of the material, there exists no cohesive zone at all. When the maximum stress exceeds the cohesive strength, the deformation in the electrode starts to localize into an array of cohesive zones (Fig. 1). Such localized deformation is thought to be initially reversible, and crack nucleation is assumed to occur only when the maximum surface separation within the cohesive zone reaches a critical value. We will focus on crack nucleation under the most severely loaded state, which will be shown to correspond to a steady state phase after the initial transient has passed but before the maximum stoichiometric solute concentration of the host material is reached.

2. Diffusion induced stress in a strip electrode

Fig. 1 shows a strip electrode with width $2h$ subject to insertion and extraction of an interstitial species such as Li. The electrode material is considered an isotropic linear elastic solid and the deformation is assumed quasi-static. Following an analogy between DIS (Prussin, 1961; Li, 1978; Yang, 2005; Zhang et al., 2007; Cheng and Verbrugge, 2008, 2009) and thermal stresses, the transport of solute in the strip is modeled as a concentration driven diffusion process along the thickness (y) direction of the electrode (Crank, 1980),

$$\frac{\partial c}{\partial t} = D\frac{\partial^2 c}{\partial y^2}, \tag{1}$$

where D is the diffusivity and c is the molar concentration of solute. The insertion of solute atoms into host causes a swelling transformation strain $\Omega c/3, \Omega$ being the partial molar volume of solute, which generates the following axial stress in the electrode (Timoshenko and Goodier, 1970),

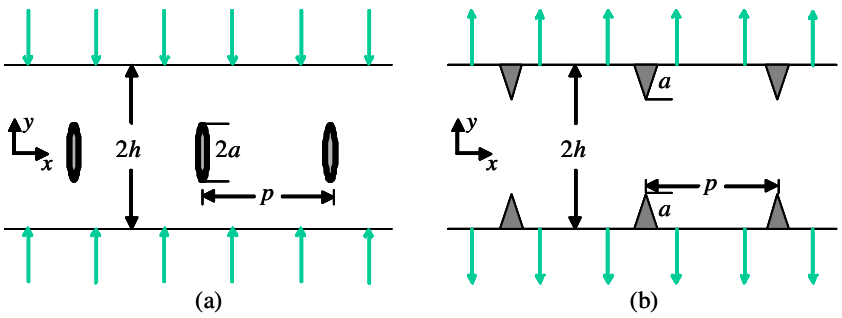

Fig. 1. Schematic illustration of crack nucleation in a strip electrode of width $2h$ during galvanostatic solute (a) intercalation and (b) extraction, modeled as diffusion along the thickness direction (y-axis). The crack nuclei are uniformly spaced with period p and modeled as cohesive zones obeying the triangular traction–separation law (Eq. (13)).

$$\sigma_D(y,t) = -\frac{E\Omega c(y,t)}{3(1-\nu)} + \frac{E\Omega}{6(1-\nu)h}\int_{-h}^{h} c(y',t)\,dy' + \frac{E\Omega y}{2(1-\nu)h^3} \times \int_{-h}^{h} y' c(y',t)\,dy', \tag{2}$$

where E is the Young's modulus and ν is the Poisson ratio of the material.

We consider the variations of solute concentration and the corresponding DIS during charging and discharging. The initial solute concentration in the electrode is assumed to be zero. Under galvanostatic boundary conditions as shown in Fig. 1,

$$-D\frac{\partial c}{\partial y}\Big|_{h} = D\frac{\partial c}{\partial y}\Big|_{-h} = -\frac{I}{F}, \tag{3}$$

where I is the surface current density and $F = 96486.7$ C/mol is Faraday's constant, the solute concentration during insertion can be found as (Crank, 1980)

$$\frac{c(y,t)}{Ih/FD} = \frac{Dt}{h^2} + \frac{3y^2-h^2}{6h^2} - \frac{2}{\pi^2}\sum_{n=1}^{\infty}\frac{(-1)^n}{n^2}\cos\left(\frac{n\pi y}{h}\right)\exp\left\{-\frac{Dn^2\pi^2 t}{h^2}\right\}, \tag{4}$$

and the associated DIS is

$$\sigma_D(y,t) = \frac{E\Omega}{3(1-\nu)}\frac{Ih}{FD} \times \left[\frac{h^2-3y^2}{6h^2} + \frac{2}{\pi^2}\sum_{n=1}^{\infty}\frac{(-1)^n}{n^2}\cos\left(\frac{n\pi y}{h}\right)\exp\left\{-\frac{Dn^2\pi^2 t}{h^2}\right\}\right]. \tag{5}$$

At the end of charging, the stress approaches a steady state while the solute concentration rises steadily with time. This situation persists until the saturation limit of material is reached. The steady state solution then acts as the initial condition for the extraction process,

$$c(y,0) = c_1 + \frac{Ih}{FD}\left[\frac{3y^2-h^2}{6h^2}\right], \tag{6}$$

where

$$c_1 = \frac{It_c}{Fh}, \tag{7}$$

t_c denoting the charging time. During extraction, the solute concentration evolves as

$$\frac{c(y,t)-c_1}{Ih/FD} = -\frac{Dt}{h^2} - \frac{3y^2-h^2}{6h^2} + \frac{4}{\pi^2}\sum_{n=1}^{\infty}\frac{(-1)^n}{n^2}\cos\left(\frac{n\pi y}{h}\right)\exp\left\{-\frac{Dn^2\pi^2 t}{h^2}\right\} \tag{8}$$

with the associated DIS

$$\sigma_D(y,t) = \frac{E\Omega}{3(1-\nu)}\frac{Ih}{FD} \times \left[\frac{3y^2-h^2}{6h^2} - \frac{4}{\pi^2}\sum_{n=1}^{\infty}\frac{(-1)^n}{n^2}\cos\left(\frac{n\pi y}{h}\right)\exp\left\{-\frac{Dn^2\pi^2 t}{h^2}\right\}\right]. \tag{9}$$

Fig. 2 plots the variations of solute concentration and the associated DIS during the first charging and discharging cycle. Due to the symmetry of the problem, the results are plotted only over half of the strip width. During insertion, the solute concentration continuously rises with time (Fig. 2a) while the stress approaches a

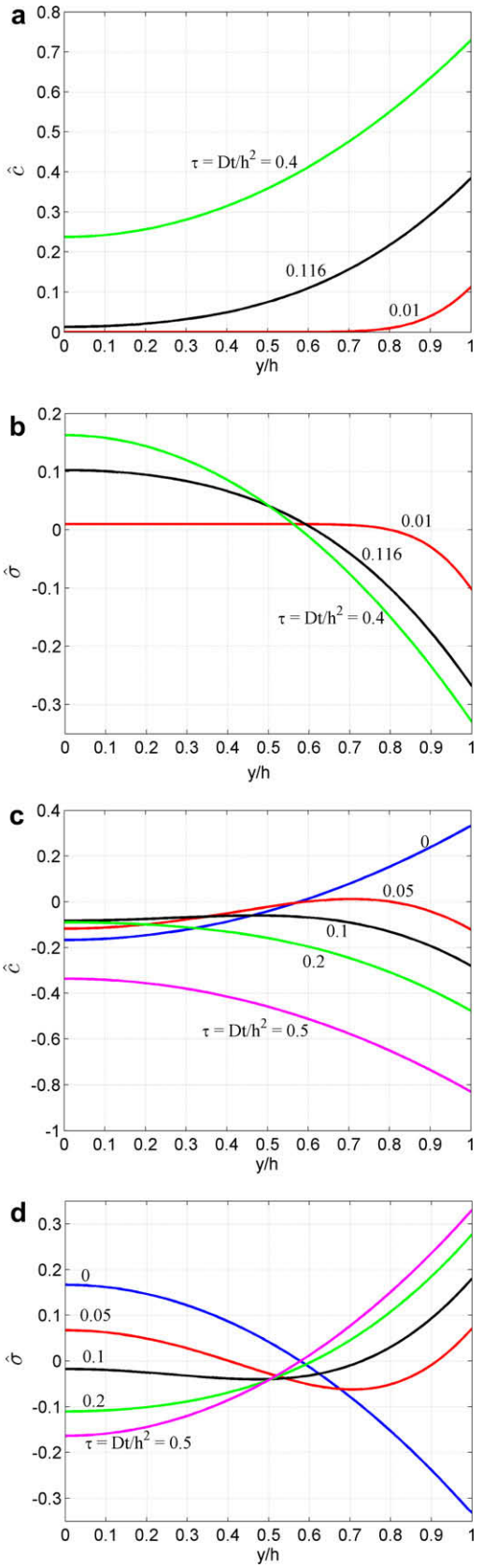

Fig. 2. Snapshot profiles of solute concentration and diffusion induced stress. (a) Concentration during insertion, (b) DIS during insertion, (c) concentration during extraction and (d) DIS during extraction. The concentration is normalized as $\hat{c} = cFD/(Ih)$ during insertion and $\hat{c} = (c-c_1)FD/(Ih)$ during extraction (Eqs. (4) and (8)), while DIS is normalized as $\hat{\sigma} = 3(1-\nu)FD\sigma/(E\Omega Ih)$ (Eqs. (5) and (9)).

steady state with tension near the center and compression near the free surface of the electrode (Fig. 2b). The peak tensile stress occurs at the center with magnitude equal to (Fig. 2b)

$$\sigma^{I}_{\text{peak}} = E\Omega Ih/18(1-\nu)FD \tag{10}$$

when reaching the steady state. During extraction, the surface current is reversed, and the solute concentration continuously decreases with time (Fig. 2c) while the stress approaches a steady state with compression near the center and tension at the surface of the electrode. In this case, the peak tensile stress at the surface reaches (Fig. 2d)

$$\sigma^{E}_{\text{peak}} = E\Omega Ih/9(1-\nu)FD \tag{11}$$

at steady state.

To appreciate the level of diffusion induced stress in high capacity electrodes, we consider silicon nanowire electrodes with an average diameter of 89 nm. Recent experiments have shown such electrodes can be charged to the near theoretical capacity of 4227 mA h g^{-1} at a charge and discharge rate of 20 h per half cycle (Chan et al., 2008), corresponding to a surface current density of $I = 0.011$ A/m^2. With concentration change in Li_xSi from $x = 0$ to 4.4, reaching a volume change as large as 59%, the partial molar volume of Li can be estimated as (Zhang et al., 2007)

$$\Omega = \frac{4}{4.4c_{\max}} = 2\times 10^{-5}\ \text{m}^3/\text{mol} \tag{12}$$

where $c_{\max} = 2.0152\times 10^4$ mol/m^3 is the stoichiometric maximum concentration of Li (Boukamp et al., 1981). Other material properties are listed in Table 1. If the lower limit of Young's modulus of fully lithiated Si is used, the peak tensile stress is estimated to be 0.1 GPa during Li insertion and 0.2 GPa during Li extraction. For faster charge and discharge rates, the nanowire electrodes begin to show irreversible capacity losses even during the first cycle (Chan et al., 2008). For example, at the charge and discharge rate of 5 h per half cycle, there is an irreversible capacity loss at the first cycle, but the capacity is then stabilized at 3500 mA h g^{-1} for the subsequent 20 cycles (Chan et al., 2008). In this case, the surface current density is $I = 0.036$ A/m^2, corresponding to a peak stress of 0.35 GPa during Li insertion and 0.7 GPa during Li extraction.

The above estimated peak tensile stresses are close to the theoretical strength of pure silicon and have most likely exceeded the cohesive strength of lithiated silicon. Why can the Si nanowires sustain such extreme mechanical stresses without fracture? In the following section, we consider crack nucleation under diffusion induced stresses in an initially crack-free electrode.

3. Cohesive model of crack nucleation in the strip electrode

Fig. 1 shows an emergent array of cohesive zones in the initially crack-free electrode. The cohesive zones are uniformly spaced at a period of p near the center of the electrode during solute insertion and at the edge of the electrode during solute extraction. The cohesive zone is assumed to obey the triangular traction–separation ($\sigma-\delta$) law (Camacho and Ortiz, 1996),

$$\sigma = \begin{cases} \sigma_c(1-\delta/\delta_c) & \delta \leqslant \delta_c, \\ 0 & \delta > \delta_c, \end{cases} \tag{13}$$

where σ_c is the cohesive strength of the electrode material and δ_c is the maximum range of cohesive interaction. The fracture energy of the material, $\Gamma = \sigma_c\delta_c/2$, is assumed to be a material constant typically on the order of surface energy in the absence of significant plastic deformation.

The emergent cohesive zones are modeled as continuous distributions of infinitesimal dislocations (Bilby and Eshelby, 1968). During solute insertion, the cohesive zones would develop at the center of the electrode as soon as the stress exceeds the cohesive strength. Within the cohesive zone, the traction and the surface separation follows Eq. (13), i.e.

$$\sigma_D(y,t) + \int_{-a}^{a} P(y,\eta)B(\eta,t)\,d\eta = \sigma_c\left(1-\frac{\sigma_c}{2\Gamma}\int_{y}^{a} B(\eta,t)\,d\eta\right), \quad -a \leqslant y \leqslant a \tag{14}$$

where the first term $\sigma_D(y,t)$ is the diffusion induced stress and the second term is the stress associated with localized deformation within the cohesive zones modeled as continuous distributions of infinitesimal dislocations with density $B(\eta,t)$ satisfying

$$\int_{-a}^{a} B(\eta,t)\,d\eta = 0. \tag{15}$$

The kernel function $P(y,\eta)$ in Eq. (14) corresponds to the axial stress at location $(0,y)$ induced by an array of edge dislocations of unit Burgers vector in the x-direction, located at position η along the y-axis and periodically distributed along the x-axis with a period equal to p. The expression for $P(y,\eta)$ is given in Appendix A. Similar to the Dugdale model (Dugdale, 1960), the cohesive zone size is determined based on the condition that there exists no singularity at the tip of the cohesive zone,

$$\lim_{\eta\to a} B(\eta,t)\sqrt{a-\eta} = 0, \tag{16}$$

and crack nucleation is assumed to occur when the maximum surface separation reaches $\delta_c = 2\Gamma/\sigma_c$, i.e.

$$\int_{0}^{a} B(\eta,t)\,d\eta = 2\Gamma/\sigma_c. \tag{17}$$

Finally, the spacing p between the cohesive zones will be determined by the condition that the stress everywhere in the electrode must not exceed the cohesive strength.

During solute extraction, the tensile stress region is shifted to the surface of the electrode while the center of the electrode is under compression. Therefore, in this case the emergent cohesive zones are placed periodically along the edge of the electrode with governing equation

$$\sigma_D(y,t) + \int_{h-a}^{h} [P(y,\eta)-P(y,-\eta)]B(\eta,t)\,d\eta = \sigma_c\left(1+\frac{\sigma_c}{2\Gamma}\int_{h-a}^{y} B(\eta,t)\,d\eta\right), \quad h-a \leqslant y \leqslant h. \tag{18}$$

In this case, the size of the cohesive zones is determined based on

$$\lim_{\eta\to h-a} B(\eta,t)\sqrt{\eta-h+a} = 0, \tag{19}$$

and the corresponding crack nucleation condition is

Table 1
Material properties of Si and operating parameters.

Parameter	Symbol (dimension)	Value	Source
Young's modulus (lithiated Si)	E (GPa)	30–80	
Poisson's ratio	ν	0.22	Freund and Suresh (2003)
Diffusion coefficient	D (m^2/s)	2×10^{-18}	Laforge et al. (2008)
Stoichiometric maximum concentration	$c_{\max}$(mol/m^3)	2.0152×10^4	Boukamp et al. (1981)
Fracture energy	Γ (J/ m^2)	2	

$$\int_h^{h-a} B(\eta,t)\,d\eta = 2\Gamma/\sigma_c. \tag{20}$$

Normalizing all stress variables by σ_c and all length variables by h in Eqs. (5), (9) and (14)–(20), we can identify a characteristic length scale as

$$\ell_{ft} = \left\{\frac{\Gamma(1-\nu)F^2D^2}{E(1+\nu)\Omega^2I^2}\right\}^{1/3}. \tag{21}$$

4. Localization spacing p

In the present cohesive model, the deformation in the electrode is spontaneously localized into a periodic array of cohesive zones along the length of the strip if the peak DIS in the electrode exceeds the cohesive strength of material. The strain localization leads to stress relaxation in the vicinity of each cohesive zone. Therefore, the post-localization stress distribution depends on the localization spacing p. If the localization spacing is too large, the stress between two adjacent cohesive zones will not be brought down to the level of cohesive strength. Oppositely, if the localization spacing is too small, the region between two adjacent cohesive zones will be over-shielded such that the maximum stress falls below the cohesive strength. This is illustrated in Fig. 3 with contour plots of axial stress in the electrode for the cohesive zone length $a/h = 0.7$. Due to the symmetry of the problem, the results are plotted only over a quarter of the region between two adjacent cohesive zones. When the cohesive zones are too widely spaced, as shown in Fig. 3b for $p/h = 5$, the maximum stress in the intermediate region between two adjacent cohesive zones is greater than the cohesive strength. When the cohesive zones are too narrowly spaced, as shown in Fig. 3c for $p/h = 1$, the stress in the intermediate region is over-relaxed to below the cohesive strength. We assume that the localization process would naturally select the cohesive zone spacing such that the maximum stress in the region between two adjacent cohesive zones is exactly equal to the cohesive strength σ_c. In the case shown in Fig. 3, this critical spacing is found to be $p/h = 2.36$ (method to determine p/h will be discussed shortly), as can be seen in Fig. 3a.

For the formation of center cohesive zones during solute insertion (Fig. 1a), the maximum axial stress in the region between two adjacent cohesive zones occurs along the axis of the strip right in the middle of the two localization zones. Hence, in this case the cohesive zone spacing p is determined by solving

$$\sigma_x(p/2,0) = \sigma_D(0,t) + \int_{-a}^{a} H(p/2,0,\eta)B(\eta,t)\,d\eta = \sigma_c \tag{22}$$

together with Eqs. (14)–(17). The kernel function $H(x,y,\eta)$ corresponds to the axial stress at (x,y) induced by an array of edge dislocations of unit Burgers vector in the x-direction located at position η along the y-axis and periodically distributed along the x-axis with a period equal to p. The expression for kernel function $H(x,y,\eta)$ is given in Appendix A. For a given cohesive strength σ_c, we solve Eqs. (14)–(17), followed by checking Eq. (22) and employing the method of bisection to determine p.

For the formation of edge cohesive zones during solute extraction (Fig. 1b), the maximum axial stress in the region between two adjacent cohesive zones occurs along the free surface at the midpoint between the two localization zones. The cohesive zone spacing p is then determined by solving

$$\sigma_x(p/2,h) = \sigma_D(h,t) + \int_{h-a}^{h} [H(p/2,h,\eta) - H(p/2,h,-\eta)]B(\eta,t)\,d\eta = \sigma_c \tag{23}$$

together with Eqs. (18)–(20). Fig. 4a and b plot the cohesive zone spacing as a function of the cohesive strength during solute insertion and extraction, respectively.

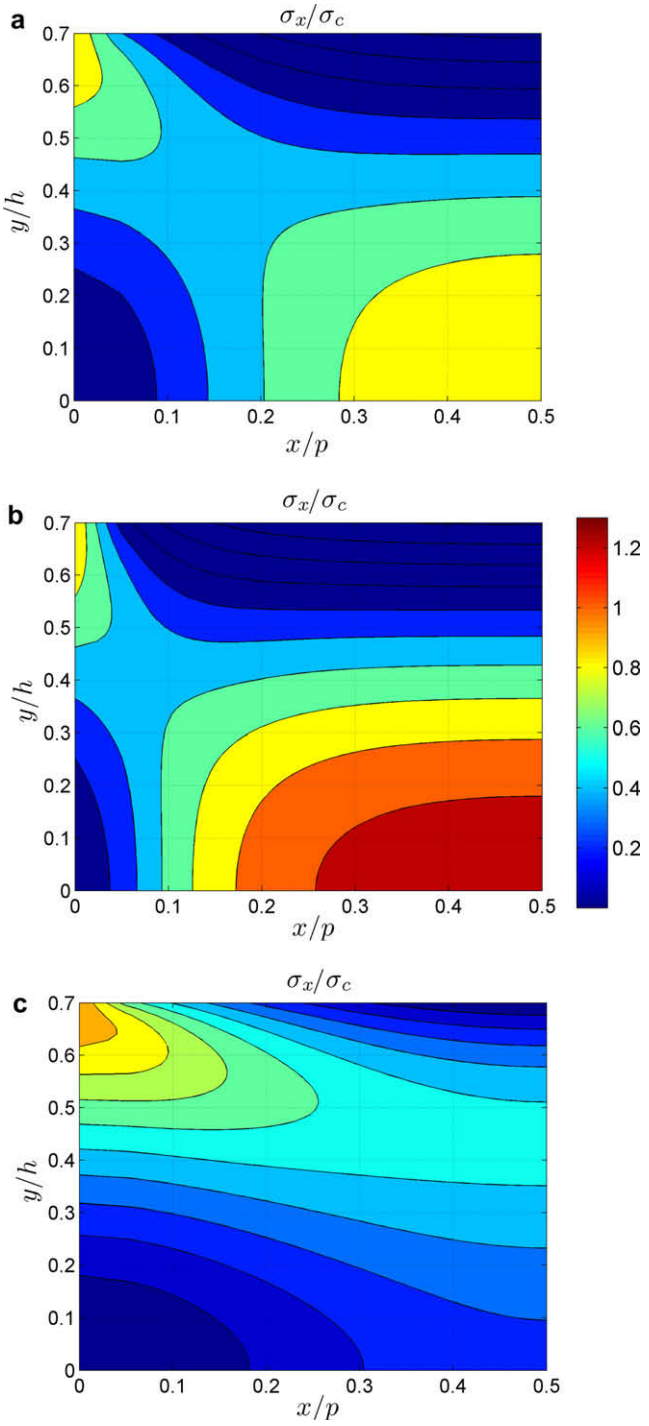

Fig. 3. Effect of localization spacing p on the distribution of axial stress σ_x in the region between two adjacent cohesive zones of length $a/h = 0.7$. (a) At the spontaneous localization spacing $p/h = 2.36$, the maximum axial stress between two adjacent localization zones is equal to the cohesive strength σ_c. (b) If the localization spacing is taken to be $p/h = 5$, the maximum axial stress between two adjacent localization zones is seen to be greater than the cohesive strength σ_c. (c) If the localization spacing is taken to be $p/h = 1$, the maximum axial stress between two adjacent localization zones is seen to be lower than the cohesive strength σ_c.

5. Critical conditions for crack nucleation

Once the localization spacing p is determined, the critical conditions for crack nucleation are obtained from Eqs. (14)–(17) for center cracks during solute insertion and from Eqs. (18)–(20) for edge cracks during solute extraction by a numerical scheme detailed in

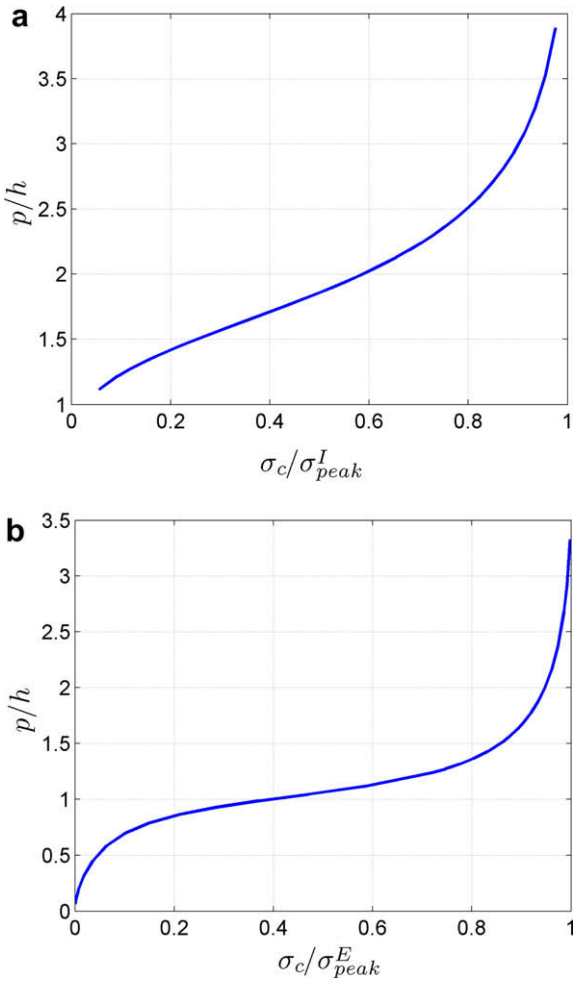

Fig. 4. Localization spacing p as a function of the normalized cohesive strength for the formation of (a) center cohesive zones during solute insertion and (b) edge cohesive zones during solute extraction. In both (a) and (b), the cohesive strength σ_c is normalized by the peak stresses $\sigma^I_{\text{peak}} = E\Omega Ih/[18(1-\nu)FD]$ during solute insertion and $\sigma^E_{\text{peak}} = E\Omega Ih/[9(1-\nu)FD]$ during solute extraction.

Appendix B. The results are shown as blue solid lines relating the normalized width of the electrode and the cohesive strength scaled by the corresponding peak stress in the electrode in Fig. 5a and b. For given values of strip width and cohesive strength, crack nucleation is predicted to occur along and above the blue lines in the sense that there exist a solution with maximum surface separation within the localization zones exceeding the cohesive interaction range δ_c. If the normalized values of strip width and cohesive strength are below these lines, crack nucleation is predicted not to occur, not because of the absence of strain localization but because the maximum surface separation in the cohesive zone cannot reach δ_c. In this case, the localized deformation within the cohesive zone is fully reversible and material would recover as soon as the diffusion induced stress in the strip is reduced. For given values of the normalized cohesive strength and strip width, the corresponding sizes of cohesive zone at crack nucleation are shown as green dashed lines.

When the peak DIS exceeds the cohesive strength, corresponding to the normalized cohesive strength smaller than unity, strain localization occurs spontaneously as a periodic array of cohesive zones with spacing given by Fig. 4. When the peak DIS is smaller than the cohesive strength, corresponding to the normalized cohesive strength exceeding unity, strain localization does not occur

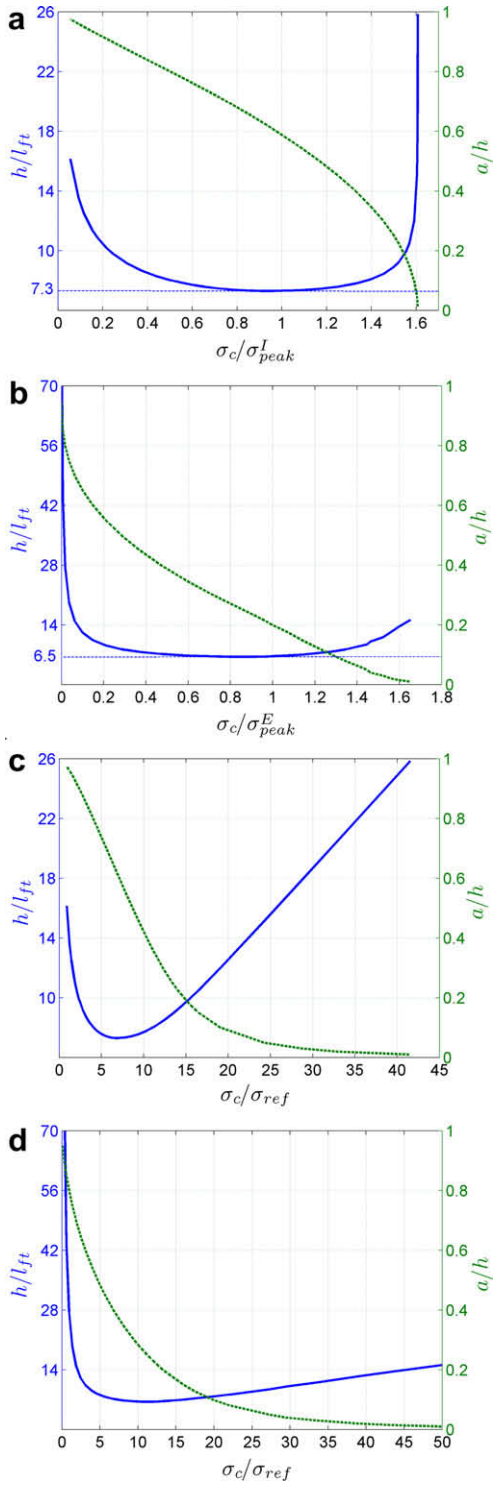

Fig. 5. The critical conditions for crack nucleation expressed as relationships between the normalized half-width of electrode, the normalized cohesive strength and the normalized critical size of cohesive zone at nucleation. The blue lines plot the critical dimension of electrode while the dashed green lines plot the critical size of cohesive zone at crack nucleation as functions of the normalized cohesive strength. (a and c) Plot the critical conditions for nucleation of center cohesive zones of length $2a$ under solute insertion while (b and d) plot those of symmetric edge cohesive zones of length a under solute extraction. In (a) and (b), the cohesive strength is normalized by the peak stresses $\sigma^I_{\text{peak}} = E\Omega Ih/[18(1-\nu)FD]$ during solute insertion and $\sigma^E_{\text{peak}} = E\Omega Ih/[9(1-\nu)FD]$ during solute extraction. In (c) and (d), the cohesive strength is normalized by the size-independent reference stress $\sigma_{\text{ref}} = E\Omega I\ell_{ft}/[18(1-\nu)FD]$ where ℓ_{ft} is the characteristic length scale defined in Eq. (21).

spontaneously. However, in this case there may exist *metastable solutions* with isolated localization zones. This type of failure may occur at locations with pre-existing defects/weaknesses. The governing equations and numerical algorithm for such metastable, isolated localizations are similar to those for spontaneous, periodic localizations, except the Green's function kernel is replaced with $K(y,\eta)$ which corresponds to the axial stress at location $(0,y)$ induced by a single edge dislocation at $(0,\eta)$ with a unit Burgers vector in the x-direction (Fotuhi and Fariborz, 2008). The expression for $K(y,\eta)$ is given in Appendix C. Fig. 5 indicates that the critical strip width and cohesive zone size transition smoothly between multiple localization to isolated localization regimes.

Most interestingly, Fig. 5 shows that, during both solute insertion and extraction, there exists a critical electrode dimension below which crack nucleation becomes impossible *irrespective of the cohesive strength of the material*. This critical dimension is found to be $h^I_{cr} = 7.3\ell_{ft}$ during solute insertion and $h^E_{cr} = 6.5\ell_{ft}$ during solute extraction; see Fig. 5a and b. Therefore, crack nucleation is more likely to occur at the surface of electrode during solute extraction, as opposed to nucleation at the center of electrode during solute insertion, even without accounting for any surface defects. In reality, stress concentration induced by surface roughness may further facilitate crack nucleation at the surface of electrodes during solute extraction. Combining these results, a critical dimension for flaw tolerant electrodes is identified as

$$2h_{ft} = 13\ell_{ft} = 13\left\{\frac{\Gamma(1-\nu)(FD)^2}{E(1+\nu)(\Omega I)^2}\right\}^{1/3}. \tag{24}$$

The significance of this equation is that it predicts an initially crack-free electrode would remain crack-free below the critical dimension. Once the electrode width exceeds this critical dimension, nucleation of surface cracks during solute extraction would become possible.

Fig. 5a and b shows that the critical dimension for flaw tolerant electrodes corresponds to the minimum width of the electrode required to prevent crack nucleation *irrespective of the cohesive strength of the material*. This is a "fail-safe" or "design for robustness" concept. If the cohesive strength of the material is known, the critical dimension of the electrode for crack nucleation may be higher than that predicted by Eq. (24). The plots in Fig. 5a and b are based on cohesive strength normalized by the peak tensile stresses during solute insertion and extraction. Since these peak stresses also depend on the electrode size, as shown in Eqs. (10) and (11), it is difficult to see from Fig. 5a and b the actual critical dimension for crack nucleation as a function of the cohesive strength. In order to decouple the effect of electrode size and cohesive strength, we introduce a size-independent reference stress $\sigma_{\text{ref}} = E\Omega I\ell_{ft}/18(1-\nu)FD$ and replot the results of Fig. 5a and b in Fig. 5c and d based on a new normalization of the cohesive strength with respect to σ_{ref}. Fig. 5c and d indicate that the critical dimension for crack nucleation increases almost linearly with cohesive strength at large values of $\sigma_c/\sigma_{\text{ref}}$. It is interesting that the critical dimension also increases at small values of $\sigma_c/\sigma_{\text{ref}}$. This is because, under the assumption of constant fracture energy $\Gamma = \sigma_c\delta_c/2$, the cohesive interaction range δ_c increases as σ_c decreases. The "fail-safe" electrode size defined in Eq. (24) corresponds a specific combination of δ_c and $\sigma_c = \sigma^*_c$ that is most susceptible to crack nucleation. When $\sigma_c > \sigma^*_c$, the electrode becomes more resistant to cracking due to higher strength of the material. In contrast, when $\sigma_c < \sigma^*_c$, the increasing resistance to cracking is due to higher interaction range δ_c, which makes it difficult to separate cohesive surfaces. In this sense, crack nucleation can be referred to as "strength-controlled" in the range $\sigma_c > \sigma^*_c$ and "separation-controlled" in the range $\sigma_c < \sigma^*_c$.

Take the material parameters listed in Table 1. For silicon nanowires electrodes to be charged to near theoretical capacity at a charge–discharge rate of 20 h per half cycle without fracture, the critical dimension for flaw tolerant electrodes, $2h_{ft}$, is estimated to be 413 nm. The nanowire electrodes adopted in experiments by Chan et al. (2008) indeed fall in this range. At faster charge–discharge rates, this critical dimension scales with increasing surface current density according to $I^{-2/3}$. For the nanowires of 89 nm in diameter adopted in experiments (Chan et al., 2008), we estimate that crack nucleation would occur at the surface of the nanowire at the charging–discharging rate of 2 h per half cycle. Indeed, the voltage profiles at different power rates show that significant capacity loss begins at the charging/discharging rate between 5 and 10 h per half cycle (Chan et al., 2008). While the reason for such capacity loss is not completely clear, the observation would be more or less consistent with our analysis if the formation of surface cracks during discharging is assumed to be a significant cause. Earlier experiments have also shown that decrepitation was suppressed in amorphous Si films about 100 nm in thickness (Graetz et al., 2003) and in amorphous Ge films around 60–250 nm in thickness (Graetz et al., 2004), leading to superior charge/discharge cycling performance compared to the bulk materials. The broad agreement between experiments and our analysis for the critical electrode dimension for crack nucleation points to the fact that crack nucleation can indeed be suppressed in nanostructured electrodes and design of fracture resistant electrodes can greatly improve the cycling performance of Li batteries.

6. Summary and discussions

In this paper, we have developed a cohesive model of crack nucleation under diffusion induced stresses in an initially crack-free strip electrode under galvanostatic solute intercalation and extraction. Our analysis shows that nanoscale size is indeed a key to suppress crack formation under large diffusion induced stresses in high capacity battery electrodes such as Si. The most important result of our analysis is that there exists a critical length scale

$$H_{ft} = 13\left\{\frac{\Gamma(1-\nu)F^2D^2}{E(1+\nu)\Omega^2I^2}\right\}^{1/3} \tag{25}$$

for the electrode to become flaw tolerant. When the characteristic dimension of the electrode is below this length scale, crack nucleation becomes impossible irrespective of the cohesive strength of material. This is not because the peak stress in the electrode remains smaller than the cohesive strength, rather it is because the maximum surface separation within an emergent cohesive zone in the electrode cannot reach the cohesive interaction range. In this case, the localized deformation in the cohesive zones is fully recoverable once the diffusion induced stresses are reduced.

Our results significantly extends and generalizes the previous analysis by Huggins and Nix (2000) who considered a bilayer plate structure in which the top layer is subjected to a swelling transformation strain e_T while the bottom layer contains a pre-existing crack. They showed that the swelling in the top layer causes a biaxial tensile stress in the bottom layer and used the Griffith criterion to predicted a critical thickness

$$H_{h-n} = \frac{23}{\pi}\left(\frac{3K_{IC}(1-\nu)}{Ee_T}\right)^2 \tag{26}$$

of the plate below which the pre-existing crack will not propagate. Here K_{IC} is the fracture toughness of the plate. Using the relation $K_{IC} = \sqrt{E\Gamma/(1-\nu^2)}$, we can rewrite the Huggins–Nix critical length as

$$H_{h-n} = \frac{207}{\pi}\frac{\Gamma(1-\nu)}{E(1+\nu)e_T^2}. \tag{27}$$

Comparing Eq. (27) and our result in Eq. (25), we can see some qualitative similarities. Both models predict that the critical electrode dimension for fracture resistant electrode should scale with the ratio between the fracture energy and Young's modulus of the material. However, the scaling is linear in the Huggins–Nix model while it is non-linear with a power index of 1/3 in our model. Furthermore, our model shows that the critical length scale for flaw tolerance should scale inversely with the density of charging current. The faster the charging, the higher the stress and the more likely the crack will be nucleated. This is consistent with experimental observations. Our model suggests that a potential design criterion for flaw tolerant electrode is

$$I^{2/3}H \leqslant \text{crit}, \tag{28}$$

where I is the operating current and H is the dimension of electrode. For a "fail-safe" design of electrode, one might first determine the allowable value of $I^{2/3}H$ by a standard testing protocol and then design the actual electrode dimension and current density according to the scaling relation in Eq. (28).

We note that the concept of flaw tolerant electrodes at nanoscale is reminiscent of biological nanocomposites such as bone in which evolution may have selected the basic structural units to be at nanoscale for flaw tolerance (Gao et al., 2003). One therefore wonders if some of the material construction strategies in nature might also help build fracture resistant electrodes in the future. For example, the self-similar hierarchical structures of bone-like materials have inspired the concept of multiscale flaw insensitivity via structural hierarchy (Gao, 2006; Yao and Gao, 2007). It has been shown that hierarchical material design could allow the nanoscale structural units to extend their flaw insensitivity properties to macroscopic size scales. Such ideas might be effectively utilized to form macroscopic electrodes based on their nanostructured units. A hierarchical composite structure similar to that of biological nanocomposites might allow electrochemically active materials to be organized at different hierarchical levels through appropriate cross-linking with soft matrices to accommodate huge volume expansions of the electrode at different scales. Current manufacturing sophistication and the encouraging performances of nanowire electrodes (Taberna et al., 2006; Chan et al., 2008) suggest that hierarchically nanostructured battery electrodes might be feasible in the foreseeable future as a promising solution to decrepitation problems in Li-ion batteries. On the other hand, chemical degradation issues may favor electrodes with minimal interface area with an electrolyte in order to minimize the formation of a solid electrolyte interface (SEI) which tends to remove active lithium ions from the charge–discharge process and contributes to capacity fading. An optimal architecture of electrodes must strike a balance between mechanical and chemical degradations.

We would like to point out a number of limitations in our current model. First, we have only considered highly idealized electrode geometry. Even for such simple geometry, we have not yet investigated the stability of the crack after it is nucleated, where it might be necessary to consider different boundary conditions on the newly formed crack surfaces (which are reported to form solid electrolyte interphase and degrade the battery performance). Second, the effect of hydrostatic stress can influence the chemical potential (Li, 1978; Yang, 2005; Zhang et al., 2007) as well as the activation energy for diffusion (Nazarov and Mikheev, 2004), introducing strongly non-linear terms in the governing equation and boundary conditions. The full coupling between stress and diffusion is expected to be important to model electrode in a strongly confined environment. Once this coupling is introduced, the crack nucleation problem will have to be treated in a more sophisticated non-linear framework, which would substantially increase the complexity of the problem. Third, the current formulation is strictly valid only in the limit of dilute solutions since otherwise the distribution of Li ions may significantly alter the physical properties of the material such as the elastic modulus. Fourth, the lithiation induced phase changes needs to be further studied. Although not treated in the current study, phase changes during lithiation are another major cause for stresses in addition to DIS. The micrometer length of electrode is important in this context, as a critical thickness of 2 μm is required for the crystallization of amorphous Si to crystalline $Li_{15}Si_4$ (Hatchard and Dahn, 2004). All these issues may significantly affect the electrode failure process in some way. Nevertheless, the simple model adopted here may serve as a first step to bring out some essential features of an appropriate length scale and the associated scaling laws for crack nucleation.

Acknowledgements

H.G.'s interest in this problem was initiated from discussions with Professor Y.T. Cheng of the University of Kentucky and Dr. Mark Verbrugge of the General Motors Research and Development Center. H.G. also acknowledges helpful discussions with Prof. William D. Nix of Stanford University. Financial support from the National Science Foundation through Grant CMMI-0758535 is gratefully acknowledged.

Appendix A. Green's function kernel (periodic case)

The Green's function kernel $P(y,\eta)$ for the periodic array of edge dislocations with a unit Burgers vector $(1,0)$ in an isotropic elastic thin strip is calculated using the superposition principle as shown in Fig. A1 The original problem is divided into two sub-problems. In the first sub-problem shown in Fig. A1a, the stress field of the periodic array of dislocations in an infinite isotropic elastic plane is determined. In the second sub-problem shown in Fig. A1b, the surface tractions $\sigma^{\infty}_{yy}(x,\pm h), \sigma^{\infty}_{xy}(x,\pm h)$ along $y=\pm h$ from the first sub-problem are negated to recover the traction free boundary conditions in the original problem. The two dimensional traction boundary value problem in the sub-problem (b) is treated using Airy stress function approach (Timoshenko and Goodier, 1970).

The stress field of a periodic array of edge dislocations with a unit Burgers vector (1,0) in an isotropic elastic infinite plane is (Hirth and Lothe, 1982)

$$\sigma^{\infty}_{x}(x,y) = \frac{E}{4p(1-\nu^2)}\left\{-\frac{\sinh(2\pi(y-\eta)/p)}{[\cosh^2(\pi(y-\eta)/p)-\cos^2(\pi x/p)]}+\frac{\pi(y-\eta)}{p}\right.$$
$$\left.\times\frac{[\cosh(2\pi(y-\eta)/p)\cos^2(\pi x/p)-\cosh^2(\pi(y-\eta)/p)]}{[\cosh^2(\pi(y-\eta)/p)-\cos^2(\pi x/p)]^2}\right\}, \tag{A1}$$

$$\sigma^{\infty}_{y}(x,y) = -\frac{E}{4(1-\nu^2)}\frac{\pi(y-\eta)}{p^2}$$
$$\times\frac{\left[\cosh(2\pi(y-\eta)/p)\cos^2(\pi x/p)-\cosh^2(\pi(y-\eta)/p)\right]}{\left[\cosh^2(\pi(y-\eta)/p)-\cos^2(\pi x/p)\right]^2}, \tag{A2}$$

$$\sigma^{\infty}_{xy}(x,y) = \frac{E}{4p(1-\nu^2)}\left\{\frac{\sin(2\pi x/p)}{2\left[\cosh^2(\pi(y-\eta)/p)-\cos^2(\pi x/p)\right]}\right.$$
$$\left.-\frac{\pi(y-\eta)}{2p}\frac{\sin(2\pi x/p)\sinh(2\pi(y-\eta)/p)}{\left[\cosh^2(\pi(y-\eta)/p)-\cos^2(\pi x/p)\right]^2}\right\}. \tag{A3}$$

The resulting non-zero tractions along $y=\pm h$ are expressed in the series form as:

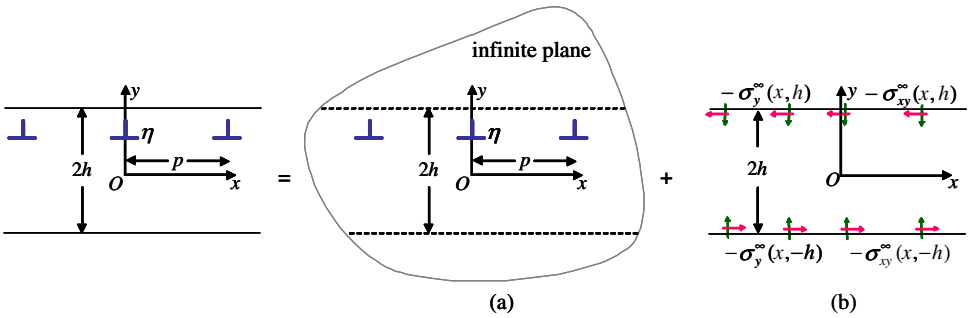

Fig. A1. A periodic array of edge dislocations with Burgers vector (1,0) located at position $(\pm np,\eta)(n=0,1,2,\ldots.)$ in an isotropic elastic strip. (a and b) Depict two sub-problems used to calculate the stress field for the original problem by the superposition principle.

$$-\left[\frac{\sigma_y^\infty(x,h)+\sigma_y^\infty(x,-h)}{2}\right]=\sum_{m=1}^{\infty}B_m\cos(2\pi mx/p), \tag{A4}$$

$$-\left[\frac{\sigma_y^\infty(x,h)-\sigma_y^\infty(x,-h)}{2}\right]=\sum_{m=1}^{\infty}C_m\cos(2\pi mx/p), \tag{A5}$$

$$-\left[\frac{\sigma_{xy}^\infty(x,h)+\sigma_{xy}^\infty(x,-h)}{2}\right]=\sum_{m=1}^{\infty}A_m\sin(2\pi mx/p), \tag{A6}$$

$$-\left[\frac{\sigma_y^\infty(x,h)-\sigma_y^\infty(x,-h)}{2}\right]=\sum_{m=1}^{\infty}D_m\sin(2\pi mx/p), \tag{A7}$$

where

$$B_m=\frac{E}{p(1-\nu^2)}\left\{\frac{\pi(h-\eta)}{2p}m\exp\left(\frac{-2m\pi(h-\eta)}{p}\right)-\frac{\pi(h+\eta)}{2p}m\exp\left(\frac{-2m\pi(h+\eta)}{p}\right)\right\}, \tag{A8}$$

$$C_m=\frac{E}{p(1-\nu^2)}\left\{\frac{\pi(h-\eta)}{2p}m\exp\left(\frac{-2m\pi(h-\eta)}{p}\right)+\frac{\pi(h+\eta)}{2p}m\exp\left(\frac{-2m\pi(h+\eta)}{p}\right)\right\}, \tag{A9}$$

$$A_m=\frac{E}{p(1-\nu^2)}\left\{\frac{\pi(h-\eta)}{2p}m\exp\left(\frac{-2m\pi(h-\eta)}{p}\right)+\frac{\pi(h+\eta)}{2p}m\exp\left(\frac{-2m\pi(h+\eta)}{p}\right)-\frac{1}{4}\exp\left(\frac{-2m\pi(h-\eta)}{p}\right)-\frac{1}{4}\exp\left(\frac{-2m\pi(h+\eta)}{p}\right)\right\}, \tag{A10}$$

$$D_m=\frac{E}{p(1-\nu^2)}\left\{\frac{\pi(h-\eta)}{2p}m\exp\left(\frac{-2m\pi(h-\eta)}{p}\right)-\frac{\pi(h+\eta)}{2p}m\exp\left(\frac{-2m\pi(h+\eta)}{p}\right)-\frac{1}{4}\exp\left(\frac{-2m\pi(h-\eta)}{p}\right)+\frac{1}{4}\exp\left(\frac{-2m\pi(h+\eta)}{p}\right)\right\}. \tag{A11}$$

To evaluate the solution to sub-problem (b), we make use of the following four auxiliary problems with boundary conditions and corresponding Airy stress function $\phi(x,y)$ (Timoshenko and Goodier, 1970) as

(i) $\sigma_y(x,\pm h)=\cos(2\alpha x)$, $\sigma_{xy}(x,\pm h)=0$,

$$\phi(x,y)=\frac{\cos(2\alpha x)}{2\alpha^2[\sinh(4\alpha h)+4\alpha h]}[-\sinh(2\alpha h)\cosh(2\alpha y)+2\alpha\{y\sinh(2\alpha y)\sinh(2\alpha h)-h\cosh(2\alpha h)\cosh(2\alpha y)\}]. \tag{A12}$$

(ii) $\sigma_y(x,\pm h)=\pm\cos(2\alpha x)$, $\sigma_{xy}(x,\pm h)=0$,

$$\phi(x,y)=\frac{\cos(2\alpha x)}{2\alpha^2[\sinh(4\alpha h)-4\alpha h]}[2\alpha y\cosh(2\alpha h)\cosh(2\alpha y)-\sinh(2\alpha y)\{\cosh(2\alpha h)+2\alpha h\sinh(2\alpha h)\}]. \tag{A13}$$

(iii) $\sigma_y(x,\pm h)=0$, $\sigma_{xy}(x,\pm h)=\sin(2\alpha x)$,

$$\phi(x,y)=\frac{\cos(2\alpha x)}{\alpha[\sinh(4\alpha h)-4\alpha h]}[-h\cosh(2\alpha h)\sinh(2\alpha y)+y\cosh(2\alpha y)\sinh(2\alpha h)]. \tag{A14}$$

(iv) $\sigma_y(x,\pm h)=0$, $\sigma_{xy}(x,\pm h)=\pm\sin(2\alpha x)$,

$$\phi(x,y)=\frac{\cos(2\alpha x)}{\alpha[\sinh(4\alpha h)+4\alpha h]}[y\sinh(2\alpha y)\cosh(2\alpha h)-h\times\sinh(2\alpha h)\cosh(2\alpha y)]. \tag{A15}$$

Application of Eqs. (A12)–(A15) to the traction boundary condition given in Eqs. (A4)–(A7) leads to the solution to sub-problem (b). Finally, combined with the solution of sub-problem (a) in Eqs. (A1)–(A3) and removing the mean axial stress in the strip, the axial stress component (σ_x) at location (x,y), denoted by $H(x,y,\eta)$, is found to be

$$\begin{aligned}H(x,y,\eta)=&\frac{E}{4p(1-\nu^2)}\left\{-\frac{\sinh(2\pi(y-\eta)/p)}{[\cosh^2(\pi(y-\eta)/p)-\cos^2(\pi x/p)]}+\frac{\pi(y-\eta)}{p}\frac{[\cosh(2\pi(y-\eta)/p)\cos^2(\pi x/p)-\cosh^2(\pi(y-\eta)/p)]}{[\cosh^2(\pi(y-\eta)/p)-\cos^2(\pi x/p)]^2}\right\}\\&+\sum_{m=1}^{\infty}\frac{2B_m\cos(2m\pi x/p)}{[\sinh(4m\pi h/p)+4m\pi h/p]}[\cosh(2m\pi y/p)\{\sinh(2m\pi h/p)-2m\pi h\cosh(2m\pi h/p)/p\}+2m\pi y\sinh(2m\pi y/p)\sinh\times(2m\pi h/p)/p\}]+\sum_{m=1}^{\infty}\frac{2C_m\cos(2m\pi x/p)}{[\sinh(4m\pi h/p)-4m\pi h/p]}[\sinh(2m\pi y/p)\times\{\cosh(2m\pi h/p)-2m\pi h\sinh(2m\pi h/p)/p\}+2m\pi y\cosh(2m\pi y/p)\cosh(2m\pi h/p)/p\}]\\&+\sum_{m=1}^{\infty}\frac{4A_m\cos(2m\pi x/p)}{[\sinh(4m\pi h/p)-4m\pi h/p]}[\sinh(2m\pi y/p)\{\sinh(2m\pi h/p)-m\pi h\cosh(2m\pi h/p)/p\}+m\pi y\cosh(2m\pi y/p)\times\sinh(2m\pi h/p)/p\}]+\sum_{m=1}^{\infty}\frac{4D_m\cos(2m\pi x/p)}{[\sinh(4m\pi h/p)+4m\pi h/p]}\times[\cosh(2m\pi y/p)\{\cosh(2m\pi h/p)-m\pi h\sinh(2m\pi h/p)/p\}+m\pi y\sinh(2m\pi y/p)\cosh(2m\pi h/p)/p\}]\\&-\frac{E}{2p(1-\nu^2)}\frac{\eta}{h}-\frac{3E}{4p(1-\nu^2)}\frac{y(\eta^2-h^2)}{h^3}.\end{aligned} \tag{A16}$$

The Green's function $P(y,\eta)$ is obtained by substituting $x=0$ into Eq. (A16),

$$P(y,\eta)=\frac{E}{4p(1-\nu^2)}\left\{-2\coth(\pi(y-\eta)/p)+\pi(y-\eta)\operatorname{csch}^2(\pi(y-\eta)/p)/p\right\}+\sum_{m=1}^{\infty}\frac{2B_m}{[\sinh(4m\pi h/p)+4m\pi h/p]}[\cosh(2m\pi y/p)\{\sinh(2m\pi h/p)$$

$$-2m\pi h\cosh(2m\pi h/p)/p\}+2m\pi y\sinh(2m\pi y/p)\sinh(2m\pi h/p)/p\}]$$
$$+\sum_{m=1}^{\infty}\frac{2C_m}{[\sinh(4m\pi h/p)-4m\pi h/p]}[\sinh(2m\pi y/p)\{\cosh(2m\pi h/p)$$
$$-2m\pi h\sinh(2m\pi h/p)/p\}+2m\pi y\cosh(2m\pi y/p)\cosh(2m\pi h/p)/p\}]$$
$$+\sum_{m=1}^{\infty}\frac{4A_m}{[\sinh(4m\pi h/p)-4m\pi h/p]}[\sinh(2m\pi y/p)\{\sinh(2m\pi h/p)$$
$$-m\pi h\cosh(2m\pi h/p)/p\}+m\pi y\cosh(2m\pi y/p)\sinh(2m\pi h/p)/p\}]$$
$$+\sum_{m=1}^{\infty}\frac{4D_m}{[\sinh(4m\pi h/p)+4m\pi h/p]}[\cosh(2m\pi y/p)\{\cosh(2m\pi h/p)$$
$$-m\pi h\sinh(2m\pi h/p)/p\}+m\pi y\sinh(2m\pi y/p)\cosh(2m\pi h/p)/p\}]$$
$$-\frac{E}{2p(1-\nu^2)}\frac{\eta}{h}-\frac{3E}{4p(1-\nu^2)}\frac{y(\eta^2-h^2)}{h^3}. \tag{A17}$$

Appendix B. Numerical scheme

Here we outline the numerical algorithm adopted to solve Eqs. (14)–(20), where the localization spacing p and the cohesive zone size a are treated as input parameters while the corresponding normalized cohesive strength and critical strip thickness are calculated as the results.

For crack nucleation at the center of electrode during solute intercalation (Fig. 1a), the length dimension in Eqs. (14)–(17) is normalized as

$$\hat{y}=\frac{y}{a},\quad \hat{\eta}=\frac{\eta}{a}, \tag{B1}$$

both defined over $[-1,1]$ to facilitate numerical analysis. The singular nature of dislocation density at both crack-tips can be represented as

$$B(\hat{\eta},t)=\frac{R(\hat{\eta},t)}{\sqrt{1-\hat{\eta}^2}}, \tag{B2}$$

where $R(\hat{\eta},t)$ is a smooth function of $\hat{\eta}$. Integrals involving square root singularity are evaluated using the Gauss–Chebyshev quadrature as (Erdogan et al., 1973),

$$\int_{-1}^{1}\frac{f(\hat{\eta})}{\sqrt{1-\hat{\eta}^2}}\,d\hat{\eta}\cong\frac{\pi}{N}\sum_{j=1}^{N}f(\hat{\eta}_j), \tag{B3}$$

where $\hat{\eta}_j=\cos((j-0.5)\pi/N), j=1,..,N$ are integration points. Eq. (14) is imposed at $N-1$ collocation points given by $\hat{y}_i=\cos(i\pi/N), i=1,\ldots,N-1$. The condition of removal of singularity in Eq. (16) becomes $R(\pm1,t)=0$, which can be expressed in terms of the integration point values of R using Krenk's extrapolation formulae (Krenk, 1975),

$$R(1,t)=\frac{1}{N}\sum_{j=1}^{N}\frac{\sin[(N-0.5)(j-0.5)\pi/N]}{\sin[(j-0.5)\pi/(2N)]}R(\hat{\eta}_j,t), \tag{B4}$$

$$R(-1,t)=\frac{1}{N}\sum_{j=1}^{N}\frac{\sin[(N-0.5)(j-0.5)\pi/N]}{\sin[(j-0.5)\pi/(2N)]}R(\hat{\eta}_{N+1-j},t). \tag{B5}$$

For crack nucleation near an edge of electrode during solute extraction (Fig. 1b), the length dimensions in Eqs. (18)–(20) are normalized over $[-1,1]$ as

$$\hat{y}=\frac{2y+a-2h}{a},\quad \hat{\eta}=\frac{2\eta+a-2h}{a}. \tag{B6}$$

The singular nature of dislocation density at the crack-tip can be represented as

$$B(\hat{\eta},t)=R(\hat{\eta},t)\sqrt{\frac{1-\hat{\eta}}{1+\hat{\eta}}} \tag{B7}$$

where $R(\hat{\eta},t)$ is a smooth function of $\hat{\eta}$. Integrals involving $\sqrt{(1-\hat{\eta})/(1+\hat{\eta})}$ can be evaluated using Gauss–Chebyshev quadrature as (Erdogan et al., 1973),

$$\int_{-1}^{1}f(\hat{\eta})\sqrt{\frac{1-\hat{\eta}}{1+\hat{\eta}}}d\hat{\eta}\cong\frac{2\pi}{2N+1}\sum_{j=1}^{N}\left[1-\cos\left(\frac{2j\pi}{2N+1}\right)\right]f(\hat{\eta}_j), \tag{B8}$$

where $\hat{\eta}_j=\cos(2j\pi/(2N+1)), j=1,\ldots,N$ are integration points. Eq. (18) is imposed at N collocation points given by $\hat{y}_i=\cos((2i-1)\pi/(2N+1)), i=1,\ldots,N$. Eq. (19) representing the condition of removal of singularity translates to $R(-1,t)=0$, which can be expressed in terms of the integration point values of R using Krenk's extrapolation formula (Krenk, 1975),

$$R(-1,t)=\frac{2}{2N+1}\sum_{j=1}^{N}\cot\left[\frac{(j-0.5)\pi}{(2N+1)}\right]\sin\left[\frac{N(2j-1)\pi}{(2N+1)}\right]R(\hat{\eta}_{N+1-j},t). \tag{B9}$$

The triangular cohesive law (Eq. (13)) introduces non-linearity in Eqs. (14) and (18) and we solve Eqs. (14)–(17) and (18)–(20) iteratively using Newton–Raphson method until convergence is achieved. In most cases, convergence is obtained within six to eight iterations.

Appendix C. Green's function kernel for a single dislocation in a strip

The Green's function kernel $K(y,\eta)$ for a single edge dislocation with a unit Burgers vector $(1,0)$ in a thin strip can be obtained from Appendix A by letting the period between dislocation approach to infinity. An alternative form of the solution has been given by Fotuhi and Fariborz (2008), which is found to be consistent with the solution given in Appendix A. Here we list the alternative solution by Fotuhi and Fariborz (2008):

$$K(y,\eta)=\begin{cases}\frac{E}{4\pi(1-\nu^2)}\frac{1}{y-\eta}+\frac{1}{h}\int_0^\infty[f_{xx1}(0,y,\eta,\alpha)\\ \quad -f^\infty_{xx1}(0,y,\eta,\alpha)]\,d\alpha \quad \eta\leqslant y\leqslant h,\\ \frac{E}{4\pi(1-\nu^2)}\frac{1}{y-\eta}+\frac{1}{h}\int_0^\infty[f_{xx2}(0,y,\eta,\alpha)\\ \quad -f^\infty_{xx2}(0,y,\eta,\alpha)]\,d\alpha \quad -h\leqslant y\leqslant\eta,\end{cases}$$

$$f^\infty_{xx1}(0,y,\eta,\alpha)=\frac{E}{4\pi(1-\nu^2)}\left[2-\frac{\alpha(y-\eta)}{h}\right]\exp\left(\frac{-\alpha(y-\eta)}{h}\right),$$

$$f^\infty_{xx2}(0,y,\eta,\alpha)=\frac{E}{4\pi(1-\nu^2)}\left[-2-\frac{\alpha(y-\eta)}{h}\right]\exp\left(\frac{\alpha(y-\eta)}{h}\right),$$

$$\frac{\pi}{4\mu}f_{xx1}(0,y,\eta,\alpha)=\frac{1}{\Delta}\{-2A_{1b_x}[\sinh\alpha(y/h-1)+\alpha(y/h-1)\cosh\alpha(y/h-1)]+2C_{1b_x}[2\cosh\alpha(y/h-1)+\alpha(y/h-1)\sinh\alpha(y/h-1)]\},$$

$$\frac{\pi}{4\mu}f_{xx2}(0,y,\eta,\alpha)=\frac{1}{\Delta}\{-2A_{2b_x}[\sinh\alpha(y/h+1)+\alpha(y/h+1)\cosh\alpha(y/h+1)]+2C_{2b_x}[2\cosh\alpha(y/h+1)+\alpha(y/h+1)\sinh\alpha(y/h+1)]\},$$

$$A_{1b_x}=L_5(L_2S_6+L_5S_7+L_4S_8);$$
$$C_{1b_x}=L_5L_1S_7+L_1L_4S_8-L_5L_2S_5-L_2L_3S_8,$$
$$A_{2b_x}=-L_5(L_1S_6+L_5S_5+L_3S_8);$$
$$C_{2b_x}=L_5L_3S_7+L_3L_2S_6-L_5L_4S_5-L_4L_1S_6,$$
$$L_1=[-1-2\alpha\eta/h-2\alpha^2\eta^2/h^2+2\alpha^2]e^{2\alpha}+[-1+2\alpha\eta/h-2\alpha^2\eta^2/h^2+2\alpha^2]e^{-2\alpha}+(1+2\alpha)e^{2\alpha\eta/h}+(1-2\alpha)e^{-2\alpha\eta/h},$$
$$L_2=-e^{2\alpha(1+\eta/h)}-e^{-2\alpha(1+\eta/h)}+2+4\alpha^2(1+\eta/h)^2,$$
$$L_3=e^{2\alpha(1-\eta/h)}+e^{-2\alpha(1-\eta/h)}-2-4\alpha^2(1-\eta/h)^2,$$
$$L_4=[1-2\alpha\eta/h+2\alpha^2\eta^2/h^2-2\alpha^2]e^{2\alpha}+[1+2\alpha\eta/h+2\alpha^2\eta^2/h^2-2\alpha^2]e^{-2\alpha}+(-1+2\alpha)e^{2\alpha\eta/h}+(-1-2\alpha)e^{-2\alpha\eta/h},$$

$$
\begin{aligned}
L_5 &= \alpha[-2-2\alpha+2\alpha\eta^2/h^2]e^{2\alpha}+\alpha[-2+2\alpha-2\alpha\eta^2/h^2]e^{-2\alpha}\\
&\quad + 2\alpha(e^{2\alpha\eta/h}+e^{-2\alpha\eta/h}),\\
S_1 &= [-1+\kappa+2\alpha(1-\eta/h)]e^{\alpha(1-\eta/h)}\\
&\quad + [1-\kappa+2\alpha(1-\eta/h)]e^{-\alpha(1-\eta/h)},\\
S_2 &= [1+\kappa+2\alpha(1-\eta/h)]e^{\alpha(1-\eta/h)}\\
&\quad + [1+\kappa-2\alpha(1-\eta/h)]e^{-\alpha(1-\eta/h)},\\
S_3 &= [-1+\kappa+2\alpha(1+\eta/h)]e^{\alpha(1+\eta/h)}\\
&\quad + [1-\kappa+2\alpha(1+\eta/h)]e^{-\alpha(1+\eta/h)},\\
S_4 &= [-1-\kappa-2\alpha(1+\eta/h)]e^{\alpha(1+\eta/h)}\\
&\quad + [-1-\kappa+2\alpha(1+\eta/h)]e^{-\alpha(1+\eta/h)},\\
S_5 &= [-1-\kappa+2\alpha(1-\eta/h)]e^{\alpha(1-\eta/h)}\\
&\quad + [-1-\kappa-2\alpha(1-\eta/h)]e^{-\alpha(1-\eta/h)},\\
S_6 &= [1-\kappa+2\alpha(1-\eta/h)]e^{\alpha(1-\eta/h)}\\
&\quad + [-1+\kappa+2\alpha(1-\eta/h)]e^{-\alpha(1-\eta/h)},\\
S_7 &= [1+\kappa-2\alpha(1+\eta/h)]e^{\alpha(1+\eta/h)}\\
&\quad + [1+\kappa+2\alpha(1+\eta/h)]e^{-\alpha(1+\eta/h)},\\
S_8 &= [1-\kappa+2\alpha(1+\eta/h)]e^{\alpha(1+\eta/h)}\\
&\quad + [-1+\kappa+2\alpha(1+\eta/h)]e^{-\alpha(1+\eta/h)},\\
\Delta &= (L_1S_2+L_5S_1+L_3S_4)(L_2S_6+L_5S_7+L_4S_8)\\
&\quad - (L_2S_2+L_5S_3+L_4S_4)(L_1S_6+L_5S_5+L_3S_8),\\
\kappa &= 3-4\nu.
\end{aligned}
$$

The infinite integral in $K(y,\eta)$ is numerically evaluated using Gauss–Laguerre quadrature (Press et al., 1992).

References

Barenblatt, G., 1959. The formation of equilibrium cracks during brittle fracture: general ideas and hypothesis. Axially symmetric cracks. Journal of Applied Mathematics and Mechanics 23, 622–636.

Besenhard, J.O., Yang, J., Winter, M., 1997. Will advanced lithium-alloy anodes have a chance in lithium-ion batteries? Journal of Power Sources 68, 87–90.

Bilby, B.A., Eshelby, J.D., 1968. Dislocations and the theory of fracture. In: Liebowitz, H. (Ed.), Fracture, an Advanced Treatise, Microscopic and Macroscopic Fundamentals, vol. I. Academic Press, New York and London, pp. 99–182.

Boukamp, B.A., Lesh, G.C., Huggins, R.A., 1981. All-solid lithium electrodes with mixed-conductor matrix. Journal of the Electrochemical Society 128, 725–729.

Bourderau, S., Brousse, T., Schleich, D.M., 1999. Amorphous silicon as a possible anode material for Li-ion batteries. Journal of Power Sources 81–82, 233–236.

Camacho, G.T., Ortiz, M., 1996. Computational modeling of impact damage in brittle materials. International Journal of Solids and Structures 33, 2899–2938.

Chan, C.K., Peng, H., Liu, G., McIlwrath, K., Zhang, X.F., Huggins, R.A., Cui, Y., 2008. High-performance lithium battery anodes using silicon nanowires. Nature Nanotechnology 3, 31–35.

Cheng, Y.-T., Verbrugge, M.W., 2008. The influence of surface mechanics on diffusion induced stresses within spherical nanoparticles. Journal of Applied Physics 104, 083521-1–083521-6.

Cheng, Y.-T., Verbrugge, M.W., 2009. Evolution of stress within a spherical insertion electrode particle under potentiostatic and galvanostatic operation. Journal of Power Sources 190, 453–460.

Christensen, J., Newman, J., 2006a. A mathematical model of stress generation and fracture in lithium manganese oxide. Journal of the Electrochemical Society 153, A1019–A1030.

Christensen, J., Newman, J., 2006b. Stress generation and fracture in lithium insertion materials. Journal of Solid State Electrochemistry 10, 293–319.

Crank, J., 1980. The Mathematics of Diffusion. Oxford University Press.

Dahn, J.R., Zheng, T., Liu, Y., Xue, J.S., 1995. Mechanisms for lithium insertion in carbonaceous materials. Science 270, 590–593.

Dugdale, D.S., 1960. Yielding of steel sheets containing slits. Journal of the Mechanics and Physics of Solids 8, 100–104.

Erdogan, F., Gupta, G.D., Cook, T.S., 1973. Method of analysis and solutions of crack problems. In: Sih, G.C. (Ed.), Mechanics of Fracture, vol. 1. Noordhoff, Leyden, pp. 368–425.

Freund, L.B., Suresh, S., 2003. Thin Film Materials. Cambridge University Press, New York.

Fotuhi, A.R., Fariborz, S.J., 2008. Stress analysis in a cracked strip. International Journal of Mechanical Sciences 50, 132–142.

Gao, H., Ji, B., Jäger, I.L., Arzt, E., Fratzl, P., 2003. Materials become insensitive to flaws at nanoscale: lessons from nature. Proceedings of the National Academy of Sciences of the United States of America 100, 5597–5600.

Gao, H., 2006. Application of fracture mechanics concepts to hierarchical biomechanics of bone and bone-like materials. International Journal of Fracture 138, 101–137.

García, R.E., Chiang, Y.-M., Carter, W.C., Limthongkul, P., Bishop, C.M., 2005. Microstructural modeling and design of rechargeable lithium-ion batteries. Journal of the Electrochemical Society 152, A255–A263.

Graetz, J., Ahn, C.C., Yazami, R., Fultz, B., 2003. Highly reversible lithium storage in nanostructured silicon. Electrochemical and Solid-State Letters 6, A194–A197.

Graetz, J., Ahn, C.C., Yazami, R., Fultz, B., 2004. Nanocrystalline and thin film germanium electrodes with high lithium capacity and high rate capabilities. Journal of the Electrochemical Society 151, A698–A702.

Hatchard, T.D., Dahn, J.R., 2004. In situ XRD and electrochemical study of the reaction of lithium with amorphous silicon. Journal of the Electrochemical Society 151, A838–A842.

Hirth, J.P., Lothe, J., 1982. Theory of Dislocations. John Wiley & Sons, New York.

Huggins, R.A., Nix, W.D., 2000. Decrepitation model for capacity loss during cycling of alloys in rechargeable electrochemical system. Ionics 6, 57–63.

Kim, I.-S., Kumta, P.N., Blomgren, G.E., 2000. Si/TiN nanocomposites novel anode materials for Li-ion batteries. Electrochemical and Solid-State Letters 3, 493–496.

Kim, M.-H., Ahn, S.-H., Park, J.-W., Ascencio, J.A., 2006. Electrochemical characteristics of a Si/Ge multilayer anode for lithium-ion batteries. Journal of the Korean Physical Society 49, 1107–1110.

Krenk, S., 1975. On the use of the interpolation polynomial for solutions of singular integral equations. The Quarterly of Applied Mathematics 32, 479–484.

Laforge, B., Jodin-Levan, L., Salot, R., Billard, A., 2008. Study of germanium as electrode in thin-film battery. Journal of the Electrochemical Society 155, A181–A188.

Li, J.C.M., 1978. Physical chemistry of some microstructural phenomena. Metallurgical Transactions A 9, 1353–1380.

Mao, O., Turner, R.L., Courtney, I.A., Fredericksen, B.D., Buckett, M.I., Krause, L.J., Dahn, J.R., 1999. Active/inactive nanocomposites as anodes for Li-ion batteries. Electrochemical and Solid-State Letters 2, 3–5.

Mohammed, I., Liechti, K.M., 2000. Cohesive zone modeling of crack nucleation at bimaterial corners. Journal of the Mechanics and Physics of Solids 48, 735–764.

Nazarov, A.V., Mikheev, A.A., 2004. Theory of diffusion under stress in interstitial alloys. Physica Scripta T108, 90–94.

Needleman, A., 1987. A continuum model for void nucleation by inclusion debonding. Journal of Applied Mechanics 54, 525–531.

Press, W.H., Teukolsky, S.A., Vetterling, W.T., Flannery, B.P., 1992. Numerical Recipes in C. Cambridge University Press.

Prussin, S., 1961. Generation and distribution of dislocations by solute diffusion. Journal of Applied Physics 32, 1876–1881.

Taberna, P.L., Mitra, S., Poizot, P.S., Simon, P., Tarascon, J.-M., 2006. High rate capabilities Fe_3O_4-based Cu nano-architectured electrodes for lithium-ion battery applications. Nature Materials 5, 567–573.

Tarascon, J.-M., Armand, M., 2001. Issues and challenges facing rechargeable lithium batteries. Nature 414, 359–367.

Thomas, J., 2003. A spectacularly reactive cathode. Nature Materials 2, 705–706.

Timoshenko, S.P., Goodier, J.N., 1970. Theory of Elasticity. McGraw-Hill Book Company.

Tvergaard, V., Hutchinson, J.W., 1992. The relation between crack growth resistance and fracture process parameters in elastic–plastic solids. Journal of the Mechanics and Physics of Solids 40, 1377–1397.

Winter, M., Besenhard, J.O., Spahr, M.E., Novak, P., 1998. Insertion electrode materials for rechargeable lithium batteries. Advanced Materials 10, 725–763.

Yang, F., 2005. Interaction between diffusion and chemical stresses. Materials Science and Engineering: A 409, 153–159.

Yang, J., Winter, M., Besenhard, J.O., 1996. Small particle size multiphase Li-alloy anodes for lithium-ion-batteries. Solid State Ionics 90, 281–287.

Yao, H., Gao, H., 2007. Multi-scale cohesive laws in hierarchical materials. International Journal of Solids and Structures 44, 8177–8193.

Zhang, X., Shyy, W., Sastry, A.M., 2007. Numerical simulation of intercalation-induced stress in Li-ion battery electrode particles. Journal of the Electrochemical Society 154, A910–A916.